Extreme star formation in starburst galaxies

Snijders, L.

Chapter 6

Compact and diffuse PAH emission in the nuclear region of M83[1]

Abstract

The nucleus of the nearby barred spiral M83 is undergoing a vigorous burst of star formation. The morphology of this region is very complex, with numerous bright young star clusters, very prominent and patchy dust, and possibly a double nucleus. To study the properties of the young stellar populations and the surrounding ISM, the nucleus of M83 was observed in various mid-infrared narrowband filters with VISIR at the VLT. In addition, the brightest mid-infrared source was observed in various spectroscopic settings in the N- and Q-band. From the fine-structure lines, we find that the stellar population dominating the mid-infrared radiation at the brightest peak has an age in the range of 1.5 – 3.3 Myr or 6 – 7 Myr, and that the surrounding ISM is of relatively low density, $\leq 10^3$ cm^{-3}. From comparison of the 11.3 μm PAH map with a [Ne II] image, two components of PAH emission are identified, one associated with the bright star-forming knots, and another more diffuse component. The latter seems to be related to a dustlane in optical images, and has H_2 ro-vibrational line emission in the near-infrared associated with it as well. This indicates that the diffuse PAH emission probably comes from lower excitation photodissociation-like regions, where the PAH molecules are excited by soft UV and even optical photons, e.g. by more evolved B, A or even later-type stars. In a global sense, extragalactic PAH emission contains contributions from dense as well as diffuse ISM components, irradiated by different radiation fields. Interpretation of high sptial resolution data, in which individual star forming regions are resolved, is not straightforward due to the complex and varying morphology of these two components of PAH emission. In conclusion, our ground-based, high spatial resolution imaging data show that PAH emission can be used as a star formation rate (SFR) indicator, as long as the ISM structure of the object under study is similar to that of the object used for the calibration of the SFR as a function of PAH emission.

Leonie Snijders, Paul P. van der Werf & Liesbeth Vermaas

Submitted to Astronomy & Astrophysics

[1]Based on observations collected at the European Southern Observatory, Paranal, Chile, under programme no.75.B-0727(A), 77.C-0367(A), and 077.B-0528(A)

6.1 Introduction

At 4.5 Mpc, M83 (NGC 5236) is the nearest large barred spiral (Cepheid distance, Thim et al 2003). M83 lives in the Centaurus group of galaxies and deep HI images show evidence for tidal arms in the outer parts of the spiral, indicating that the spiral is interacting with its close neighbour NGC 5253 (Park et al 2001; Huchtmeier & Bohnenstengel 1981). Both NGC 5253 and the nucleus of M83 undergo a vigorous burst of star formation (Calzetti et al 1997, 1999; Tremonti et al 2001), but since the last close passage between these two galaxies took place 1 – 2 Gyr ago (van den Bergh 1980; Caldwell & Phillips 1989), it is unclear whether these starbursts are directly triggered by the interaction.

The morphology of the central 300 pc around the nucleus of M83 is extremely complex (Gallais et al 1991; Elmegreen et al 1998; Thatte et al 2000). Harris et al (2001) identified around 400 star clusters from HST images. As is frequently observed in barred spirals, most of these hotspots seem to be oriented along a circumnuclear ring, which is probably close to the Inner Lindblad Resonance (Elmegreen et al 1998). However, the whole nuclear region is affected by patchy and often large column densities of obscuring dust, hiding part of the starburst ring from view, and complicating the understanding of the morphology in general. The most prominent source in the mid-infrared and radio, which corresponds to the most active region of star formation, is offset by $\sim 4\farcs4$ to the west relative to the nucleus as determined in the optical, ($\sim$100 pc in projection at a distance of 4.5 Mpc; at this distance 1″ corresponds to 22.5 pc), at the edge of the starburst ring (Telesco 1988; Gallais et al 1991, and this work).

The presence of massive amounts of dust hide part of the action from view in the optical and even in the near-infrared. HST images show that apart from a circular window of relatively low extinction, a large fraction of the nuclear region is covered by layers of dust impenetrable by the optical radiation (Fig. 1 in Harris et al 2001). For this reason observations at longer wavelengths are crucial to study the most embedded sources.

Until recently only space-based facilities were available for observations in the mid-infrared. The data of the Infrared Space Observatory (ISO), and more recently of the Spitzer Space Telescope, gave and still give the field of research on star formation in starburst galaxies an enormous impulse. However, the data of these space telescopes do not provide sufficient spatial resolution to study the properties of individual extragalactic stellar populations. These small spatial scales can only be resolved using ground-based mid-infrared instruments mounted on large telescopes, of which the first ones have only become available to the general scientific community several years ago.

In this Chapter, we present high spatial resolution mid-infrared imaging and spectroscopy of the nuclear starburst of M83, obtained with the VLT Imager and Spectrometer for mid Infrared (VISIR, Lagage et al 2004) at ESO's VLT. Images in several narrow-band filters are used to study the spatial distribution of the PAH and [Ne II] emission in detail. Although PAH emission is generally observed to be strong in star-forming regions, the source of excitation is poorly understood. Usually the absorption of UV photons is thought to be the dominant process, but the detection of significant PAH emission from UV-poor nebulae (Uchida et al 1998; Li & Draine 2002) indicates that

lower energy optical photons can excite the PAH molecules as well. With the detailed comparison of the PAH emission and emission from H II regions ([Ne II]) the amount of PAH emission directly associated with star formation and the remaining more diffuse emission can be quantified. Furthermore, fine-structure lines detected in the N- and Q-band spectra are analysed to determine properties of the stellar populations.

In Section 6.2, a description of the observations and data reduction can be found. The resulting images and spectra are presented in Section 6.3. Section 6.4 discusses the spatial distribution of the PAH and [Ne II] emission. Spectral features from the N- and Q-band spectra are analysed in Section 6.5. Finally, the conclusions can be found in Section 6.6.

6.2 Observations and data reduction

6.2.1 VISIR narrowband imaging

In the night of April 9 2006, the starbursting nucleus of M83 was observed with VISIR at the VLT. Images were obtained in five narrowband filters; the SIV_2, PAH2_2, and NeII_2 filters to measure the continuum emission, the PAH2 filter, which contains the PAH feature at 11.25 μm, and the [Ne II] filter, which covers the [Ne II] fine-structure line at 12.81 μm (see Table 6.1 for an overview of the observations; the wavelength ranges covered by the imaging filters are indicated in the spectrum shown in Fig. 6.3). The total on-source integration time was 18 minutes in each filter. With the intermediate field pixel scale of $0\farcs127$, the 256 $\times$ 256 pixels detector gives a field of view of $32\farcs5 \times 32\farcs5$. Chopping and nodding was applied with a throw of 12"to remove the strong background radiation. Additionally, a random jitter offset $\leq$ 1"was given to the telescope between nod cycles to correct for array artifacts. Before and after the science target observations the standard stars HD91056 and HD99167 were observed for flux calibration (Cohen et al 1999).

IRAF[1] routines and customized IDL scripts were used for data reduction. Subtracting the chopping and nodding pairs removes most of the sky and telescope background. The resulting images were shifted and co-added. Any residual global background was removed by subtracting a constant value, which was measured in several 'object-free' portions of the image. Absolute flux calibration was obtained by normalizing the standard star images to VISIR narrowband fluxes. This calibration is uncertain by at least 20% based on the dispersion derived from the standard stars observed before and after the science observations.

Line maps were created by continuum-subtracting the images in the PAH and [Ne II] filters. The continuum at 11.25 μm (for the PAH map) and 12.81 μm (for [Ne II]) was estimated by making a linear interpolation between two flanking continuum filters. For the PAH map the SIV_2 and PAH2_2 continuum filters were used for this purpose, for the [Ne II] image the PAH2_2 and [Ne II]_2 filters. The resulting images and the PAH2_2 continuum map can be found in Fig. 6.2.

[1]Image Reduction and Analysis Facility (NOAO, National Optical Astronomy Observatories)

Apertures for photometry were defined around peaks in the [Ne II] image (sources 1 – 7; see Table 6.2 and Fig. 6.1 for positions and radii). Additionally, two apertures were placed at locations of significant continuum emission (sources 8 and 9). Two larger apertures were defined at regions of diffuse PAH emission (sources 10 – 11). Photometry was done by adding all flux within the apertures and subtracting a local diffuse background (additional to the local background already corrected for), which was measured in the relatively empty region northeast of the bright central source at source 1 (the black circle in Fig. 6.1).

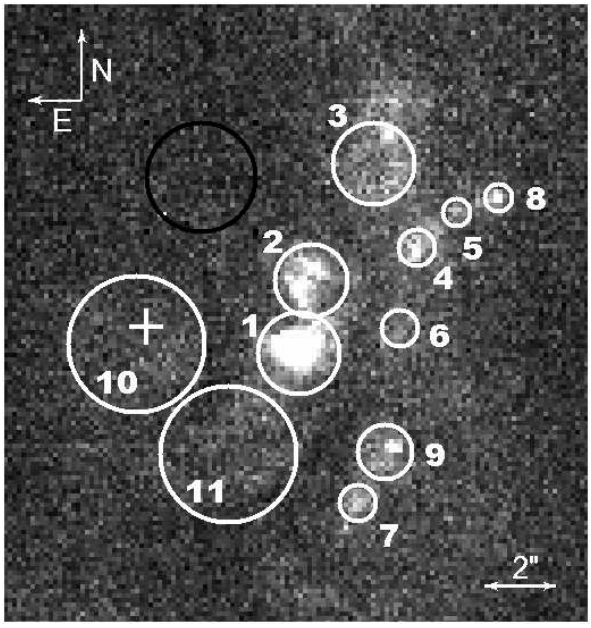

Figure 6.1 — The positions and sizes of the apertures for photometry on an image in the PAH2 filter (continuum plus PAH emission). Apertures 1 – 9 correspond to the compact knots identified in the [Ne II] and continuum images. Positions 10 and 11 correspond to regions of diffuse emission. The black aperture indicates where the local background was measured. The white cross indicates the location of the optical nucleus.

6.2.2 VISIR spectroscopy

For the brightest mid-infrared peak (source 1), low-resolution N-band spectroscopy was obtained in a 0.″75 slit in June 2005 and April 2006 . Four overlapping spectral settings were required to cover the full N-band (see Table 6.1). The total on-source integration time was 35 minutes for each spectroscopic setting. Similar to the imaging setup, chopping and nodding was applied on the slit with a 12″chop throw to correct for background emission. Early-type stars (B7 – B9.5) and a K0 giant were observed before and after the science target observations for flux calibration (HIP108085, HIP109268, HIP113963, and HIP60965, from the Hipparcos Catalogue, Perryman et al 1997, and HD123139, Cohen et al, 1999).

Medium-resolution spectroscopy around the [S III] emission line at 18.71 μm was obtained for the same source as well. The total on-source integration time was 22 minutes. The setup was identical to that applied for the N-band spectroscopy, chopping and nodding along the slit with a 12″ chopper throw. The K0 giant HD123139 was observed directly before the science observation for flux calibration.

The first steps in the data reduction were identical to those described for the imaging setup. Additionally, the spectral curvature was corrected using the prescription for the distortion as given in the VISIR manual. Wavelength calibration was done by tracing skylines. Finally, the spectrum was extracted in a 1.″91 aperture and is shown in Fig 6.3. Both from the agreement in the wavelength ranges where the spectral settings overlap (for example, the 11.4 and the 12.4 μm spectral setting overlap between 11.37 – 12.48 μm) and from the consistency of the settings that were observed twice (the 8.8 and 9.8 settings), we conclude that the flux calibration is more accurate than

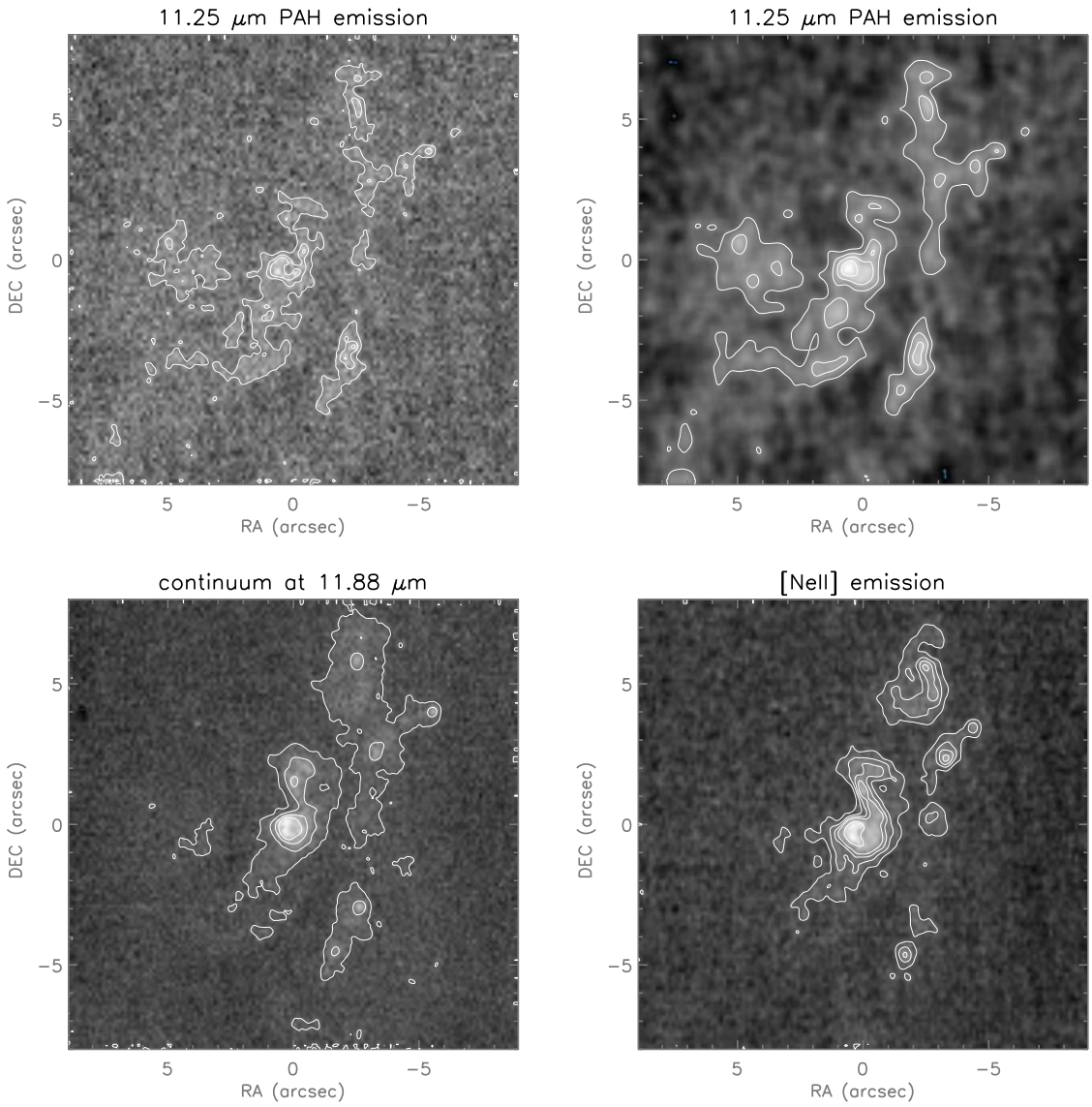

Figure 6.2 — Mid-infrared images of the nucleus of M83, all based on narrowband observations obtained with VISIR. The upper two panels show the continuum-subtracted PAH emission at 11.25 μm. *Upper left:* the PAH emission is shown after rebinning the image onto a finer grid, interpolating the pixel values in steps of 1/10 of the pixel size. The contours correspond to 1.0, 1.7, and $2.2 \cdot 10^{-13}$ erg s^{-1} cm^{-2} arcsec^{-2} (in all images the lowest contours corresponds to 5σ above the background). *Upper right:* is the same image as the upper left, but the technique of adaptive filtering is applied with a kernel of 5 pixels to remove the high frequency noise (Lorenz et al 1993). The contours in this image correspond to 0.8, 1.3, 1.7, and $2.2 \cdot 10^{-13}$ erg s^{-1} cm^{-2} arcsec^{-2}. The bottom row shows *left:* the continuum at 11.88 μm (the PAH2_2 filter, the other continuum images show similar morphology), and *right:* the continuum-subtracted [Ne II] image. Both images are rebinned in the same way as the upper left PAH map. The contours correspond to 21.7, 55.8, 93.0, and 124.0 mJy arcsec^{-2} in the continuum map and to 2.2, 3.2, 4.8, 6.0, and $9.0 \cdot 10^{-13}$ erg s^{-1} cm^{-2} arcsec^{-2} in the [Ne II] image. In all images North is up and East is left. The x- and y-axes are in arcsec and (0,0) corresponds to (α,δ)=(13 37 00.538,-29 51 54.81). The optical nucleus is located at ($\Delta\alpha$,$\Delta\delta$)=(+5.″7,+0.″85), left of the brightest mid-infrared peak in the images shown here.

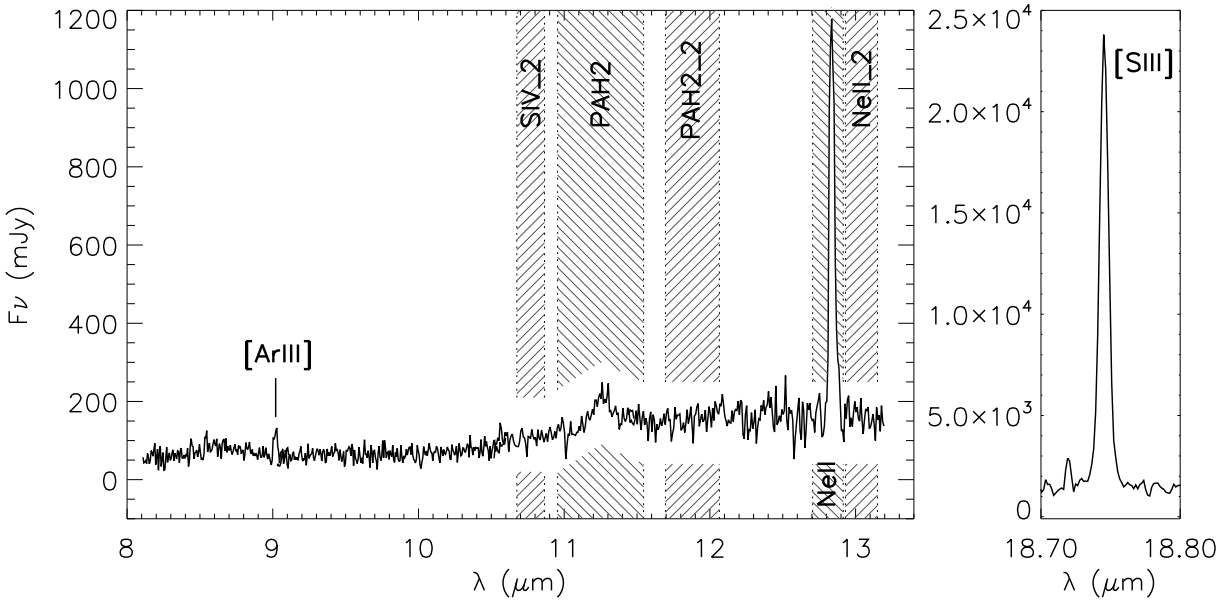

[b]

Figure 6.3 — *Left:* Low-resolution N-band spectrum of the brightest mid-infrared source in the nucleus of M83 (source 1). The dashed vertical bands indicate the wavelength range covered by the narrowband imaging filters. The names of the imaging filters are indicated as well. *Right:* Medium-resolution Q-band spectroscopy covering the range between 18.7 – 18.8 μm of the same source. The feature at 18.714 μm results from an array artefact.

15% for the N-band spectroscopy observations. The accuracy of the flux calibration for the Q-band spectrum is 20%.

Fine-structure line fluxes were measured using ISAP[1]. A gaussian distribution was fitted to the continuum-subtracted emission lines. The line fluxes were determined by integrating over these gaussian fits. The flux of the broad PAH feature was estimated by subtracting a linear interpolation of the continuum at 10.77 and 11.88 μm (which are the identical wavelengths used for the creation of the PAH image). The remaining flux from the continuum-subtracted PAH feature was determined by integrating over the same wavelength range as the PAH2 imaging filter (central wavelength = 11.25 μm,$\Delta\lambda$ = 0.57 μm; line fluxes are listed in the last row of Table 6.2).

6.2.3 SINFONI data

To discuss the excitation mechanism of the observed PAH emission, the PAH map is compared with H_2 1-0 S(1) ro-vibrational line emission (2.1218 μm) in the near-infrared. In March 2005 the nucleus of M83 was observed in the K-band with the Spectrograph for INtegral Field Observations in the Near Infrared (SINFONI, Eisenhauer et al 2003; Bonnet et al 2004) at the VLT. At the largest spatial scale of $0\farcs25$ per pixel the field of view is $8'' \times 8''$, which is not big enough to cover the whole nuclear

[1]The ISO Spectral Analysis Package is a joint development by the LWS and SWS Instrument Teams and Data Centers. Contributing institutes are CESR, IAS, IPAC, MPE, RAL and SRON.

region of M83 in one pointing. A mosaic was constructed by combining three pointings, for each of which the total on-source integration time was 10 minutes. The H_2 1-0 S(1) line map was constructed by collapsing the datacube over the line width and subtracting a linear interpolation of the continuum at 2.1187 and 2.1282 μm. More detailed information on this data set will be presented in Vermaas et al (in preparation).

6.3 Results

The images of the nucleus of M83 show a complex structure (Fig. 6.2). In all filters the images are dominated by a very bright, extended central peak (source 1; see Fig. 6.1). Emission connected to this peak extends 2"to the north (source 2), together forming the central structure shaped like a quaver symbol (eighth-note). West of the central structure, an elongated, thin, curved filament of diffuse emission can be found, which connects several relatively bright knots (sources 3 – 9). These sources form the exten-

Table 6.1 — Overview observations

VISIR imaging				
Filter	λ_{centr} (μm)	$\Delta\lambda$ (μm)	T_{int} (min)	Date
SIV_2	10.77	0.19	18	April 9 2006
PAH2	11.25	0.59	18	April 9 2006
PAH2_2	11.88	0.37	18	April 9 2006
NeII	12.81	0.21	18	April 9 2006
NeII_2	13.04	0.22	18	April 9 2006
VISIR spectroscopy				
Spectral setting	λ_{centr} (μm)	R	T_{int} (min)	Date
LR N[1]	8.8	300 – 390	35	June 16 2005 & April 8 2006
LR N[1]	9.8	305 – 360	35	June 16 2005 & April 8 2006
LR N[1]	11.4	185 – 220	35	June 16 2005
LR N[1]	12.4	215 – 250	35	June 16 2005
MR Q[1]	18.7	$\sim$1800	22	April 8 2006
SINFONI integral field spectroscopy				
Band	λ_{centr} (μm)	R	T_{int} (min)	Date
K-band	2.18	4000	10	March 23/24 2005

[1] LR N: low-resulotion N-band spectroscopy; MR Q: medium-resolution Q-band spectroscopy.

sion of the semi-circular starburst annulus identified in the near-infrared (Gallais et al 1991). Low surface brightness emission is observed in the PAH map east-southeast from the central bright peak (sources 10 and 11). The [Ne II] and continuum images only show marginal emission at these locations. As already noted sixteen years ago by Gallais et al (1991) it is remarkable how much the observed structure changes between the optical, near-infrared, mid-infrared and radio. Not only is the mid-infrared peak displaced to the west by $\sim 4\farcs4$ from the optical nucleus (indicated with a cross in Fig. 6.1), there is no significant mid-infrared emission detected from the location of the optical nucleus. The [Ne II] emission shows no signs of the presence of a significant population of massive O and B stars, only some diffuse PAH emission can be found. The average PAH surface brightness in sources 10 and 11 is $2.2 \pm 0.4 \cdot 10^{-13}$ erg s^{-1} cm^{-2} arcsec^{-2}.

In Fig. 6.4 we compare the structure observed in the mid-infrared with an optical image by overlaying a VISIR [Ne II] image in contours on an HST image in the F656N filter (F656N covers the Hα recombination line; see also Fig. 1 in Harris et al (2001) for a HST color composite). This image shows that the brightest mid-infrared peak, source 1, corresponds to a number of bright optical sources, oriented in a ring-like structure

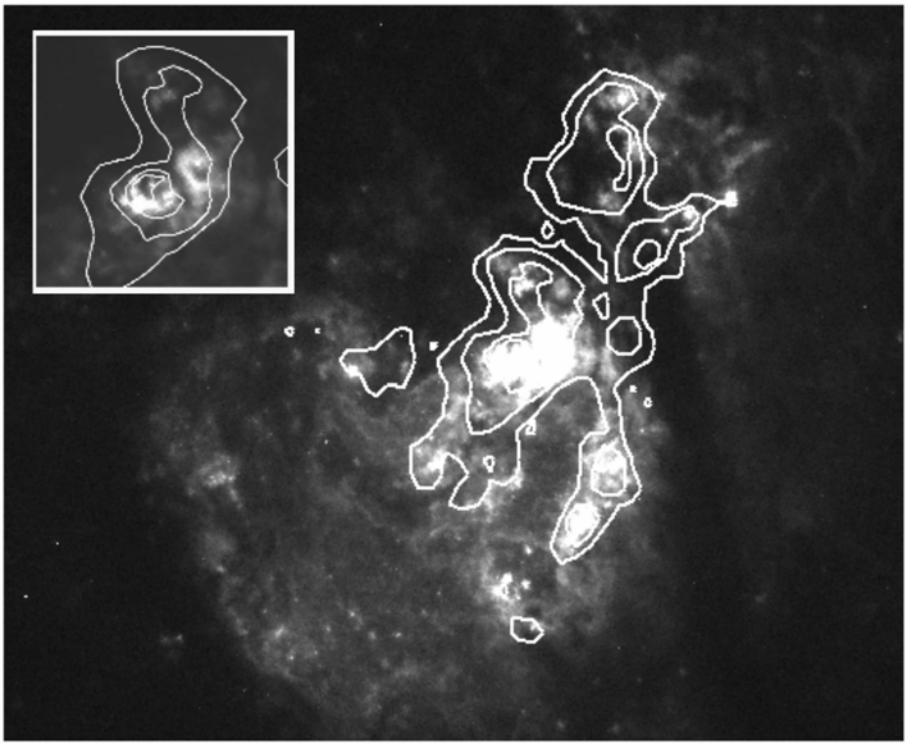

Figure 6.4 — Emission in the [Ne II] filter ([Ne II] lines emission plus continuum) overlayed in white contours on a HST F656N image (Hα emission plus continuum). The contours correspond to 1.7, 3.2, 6.9, 13.6 and $19.1 \cdot 10^{-13}$ erg s^{-1} cm^{-2} arcsec^{-2}. Astrometric calibration of the mid-infrared images is done by matching the position of the brightest peak with that of the brightest peak in the Spitzer 8 μm IRAC image. *Inserted:* a blow-up of the region around the brightest mid-infrared peak (source 1). Note how the [Ne II] emission follows the ring-like distribution observed in the F656N image. North is up, east is left.

Table 6.2 — Line fluxes

Pos	RA[1] (J2000)	DEC[1] (J2000)	Aperture radius	ID_{HST}	F_{PAH} (10^{-13} erg s^{-1} cm^{-2})	$F_{[NeII]}$ (10^{-13} erg s^{-1} cm^{-2})	PAH/[Ne II]
Compact knots[2]							
1	13 37 00.562	-29 51 55.47	1.″14	24/27/21/23/ 18/19/17	$13.6\ ^{+6.0}_{-5.2}$	22.6 ± 4.0	0.60 ± 0.26
2	13 37 00.536	-29 51 53.44	1.″02	97[3]	$6.7\ ^{+3.5}_{-3.1}$	11.3 ± 2.1	0.59 ± 0.31
3	13 37 00.401	-29 51 50.17	1.″14	7	$7.4\ ^{+3.5}_{-3.1}$	12.9 ± 2.4	0.57 ± 0.28
4	13 37 00.309	-29 51 52.51	0.″51	...	$1.8\ ^{+1.0}_{-0.8}$	3.0 ± 0.6	0.60 ± 0.32
5	13 37 00.223	-29 51 51.53	0.″38	...	$1.4\ ^{+0.4}_{-0.4}$	1.2 ± 0.2	1.18 ± 0.39
6	13 37 00.346	-29 51 54.77	0.″51	...	$2.0\ ^{+0.7}_{-0.6}$	2.2 ± 0.3	0.89 ± 0.31
7	13 37 00.435	-29 51 59.66	0.″51	13/11/15/ 16/9/22	$2.0\ ^{+0.8}_{-0.7}$	2.0 ± 0.4	0.98 ± 0.42
8	13 37 00.122	-29 51 51.13	0.″38	4	$1.0\ ^{+0.4}_{-0.4}$	0.0 ± 0.1	>9.78
9	13 37 00.377	-29 51 58.24	0.″76	8/10/9/6/ 11/12/14	$5.5\ ^{+1.8}_{-1.5}$	2.6 ± 0.7	2.09 ± 0.84
Diffuse emission[2]							
10	13 37 00.911	-29 51 55.21	1.″90		$21.0\ ^{+3.6}_{-3.4}$	5.3 ± 1.5	3.96 ± 1.30
11	13 37 00.713	-29 51 58.29	1.″90		$18.0\ ^{+3.6}_{-3.2}$	10.1 ± 1.9	1.78 ± 0.47

[1] Astrometric calibration was done by matching the brightest peak in our images with the brightest peak in the 8 μm IRAC image of the nucleus of M83.

[2] The locations of sources 1 – 7 are the peaks in the [Ne II] image. Sources 8 and 9 are (relatively) compact continuum peaks, and positions 10 and 11 correspond to region of diffuse emission. The fluxes are corrected for a local background (additional to the global background already corrected for in the reduction process). The diffuse background as measured in an aperture in the empty region northwest of position 1 is subtracted from the flux measured in these apertures (see black circle in Fig. 6.1).

[3] From Table 3 in Harris et al (2001). All other ID numbers are from Table 2 in that same paper.

(this apparent ring can also be the effect of patchy foreground extinction). Southeast of source 1, a region of relatively low extinction with hundreds of bright optical sources is found. In this area we find two mid-infrared sources corresponding to bright cluster complexes (sources 7 and 9). Furthermore, two regions of diffuse emission are identified (sources 10 and 11), which are most likely related to patches of dust seen in the optical. The area northwest of the brightest peak is dominated by a very prominent dust lane, with a handful of highly reddened sources scattered around it. Some of our mid-infrared sources clearly correspond to several of these individual optical sources (sources 5 and 8), others do not have an optical counterpart detected and seem to be deeply buried in the dust (sources 4 and 6).

The N-band spectrum of the brightest mid-infrared peak shows the characteristic features of a star-forming region. Fine-structure lines originating from the H II region are observed; strong [Ne II] emission and a clear detection of the [Ar III] line as well, both ionized by massive stars in the newly formed star cluster. Tracing regions further out from the stellar population we see PAH emission and thermal dust continuum from the photodissociation region (PDR).

Table 6.3 — Line fluxes

Species	Flux (10^{-13} erg s^{-1} cm^{-2})
[ArIII]	0.6 ± 0.1
PAH	4.6 ± 1.1
[NeII]	8.5 ± 1.3
[SIII]	15.1 ± 3.0

All in an aperture of 1.″9 with a slit width of 0.″75.

6.4 Diffuse versus compact PAH emission

Comparison of the PAH and the [Ne II] maps shows that the PAH emission traces the H II regions, which are apparent as peaks in the [Ne II] map (see Figs. 6.2 and 6.5). The central bright peak as well as the hotspots in the arc-like filament are prominent in both images. On smaller scales the PAH emission also follows the morphology seen in the [Ne II] map; both show a ring-like structure in the heart of the central bright peak. So it is clear that at least part of the PAH emission is directly coupled to the regions in which young stellar populations live.

In addition to the regions of compact PAH emission, a second component of more diffuse PAH emission can be identified (sources 10 and 11). These sources of PAH emission do not correlate with regions of ionized gas emission, but they seem to coincide with a patchy veil of dust in the HST images (see Fig. 6.4). From these locations some weak, diffuse mid-infrared continuum emission is detected as well (Fig. 6.2).

To determine which fraction of the PAH and [Ne II] emission is diffuse and what fraction originates from compact, bright, star-forming knots, we compare the combined flux measured in sources 1 – 9 with the total flux measured in all apertures together. Of the total [Ne II] flux, 79% originates from the compact knots 1 – 9, and 21% comes from sources 10 and 11. In the case of PAH emission, only 51% of the total flux originates from sources 1 – 9 combined, the other half of the total flux is diffuse. From

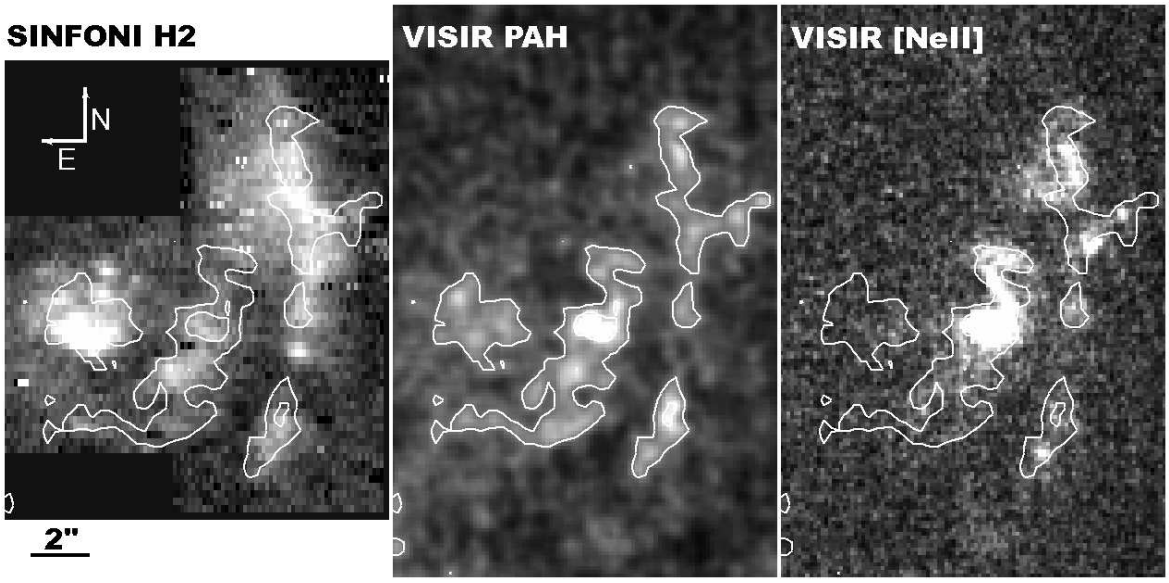

Figure 6.5 — A comparison of *left:* near-infrared H−2 1-0 S(1) emission (2.1218 μm) measured with the integral field spectrograph SINFONI, *middle:* 11.25 μm PAH emission, and *right:* 12.81 μm [Ne II] fine-structure line emisson. The contours correspond to PAH emission at 0.9 and $1.7 \cdot 10^{-13}$ erg s^{-1} cm^{-2} arcsec^{-2}. Note how the PAH eission traces the distribution in the [Ne II] emission much closer, than the H_2 emission does.

Fig. 6.1 it is clear that, although most emission is covered by the eleven apertures, some diffuse emission exists in the areas between the apertures. This component of diffuse emission in the nuclear region is estimated by adding up the pixels outside of the apertures with a flux density larger than 3σ above the background. This lowers the fraction of the total flux measured in the compact knots 1 – 9 to 60% for [Ne II] and 26% for PAH. The [Ne II] is with 60 – 80% of the total emission coming from sources 1 – 9 significantly more concentrated in the compact star-forming regions than the PAH emission, of which only 26 – 51% is directly associated with the H II regions. This is clear from visual inspection of the line maps in Fig. 6.2 as well. Another strong indication for the presence of a significant component of low surface brightness PAH emission comes from comparison of our data with the mid-infrared ISO data presented by Vogler et al (2005). In the ISO spectrum of the nucleus of M83, which covers the central $6'' \times 6''$, the equivalent width (EW) of the 11.25 μm PAH feature is 0.55 μm. Both from the N-band spectrum and from the narrowband imaging we measure an EW(PAH) of 0.19 μm. This difference shows that a component of low surface brightness exists in the central region, for which VISIR is not sensitive enough to detect, or which was removed by the relatively small chopper throw or by the global background correction (the background for the ISO spectrum was measured 7.5 – 9 arcminutes from the nucleus). Similarly low surface brightness PAH emission was found before in the comparison of space-based and ground-based spectra of super star clusters in the Antennae galaxies (NGC 4038/4039; Chapter 3 and Snijders et al 2006).

This result is consistent with the results of Pérez-González et al (2006), who evaluate various mid-infrared star formation rate (SFR) indicators. Even after subtraction of a

global diffuse background, they find that the 8 μm flux correlates with the Hα emission absorbed by dust, but with a very large scatter of the individual data points around the correlation ($\gtrsim$ 60%). The 8 μm Spitzer IRAC filter covers a portion of the spectrum with some very strong PAH features (the 7.8 and 8.6 μm features). The large scatter around the relation between the 8 μm and Hα luminosity likely arises from significant differences in the relative contribution of PAH emission in the individual apertures. This is another strong indication that PAH features cannot exclusively be connected with massive, young stars. Similar results are found by Calzetti et al (2007) as well.

If we focus on the compact star-forming knots defined by peaks in the [Ne II] map, sources 1 – 7, our data shows no evidence for PAH destruction. Unfortunately, from our data we cannot derive any information on the radiation hardness for these sources. Under the first order assumption that the radiaton of a younger, brighter H II region is harder than that of an older, fainter one, we expect the ratio of the PAH 11.25 μm flux over the [Ne II] emission line flux, F(PAH$_{11.25\mu m}$)/F([Ne II]), to drop with increasing F([Ne II]) in case of significant PAH destruction. The measured F(PAH$_{11.25\mu m}$)/F([Ne II]) ratio is consistent with being constant at a value of 0.77 $\pm$ 0.32 (see Table 6.2 and Fig. 6.6). Since we do not detect [S IV] fine-structure line emission even in the brightest peak, it is plausible that most star clusters in the nuclear region are relatively evolved, with ages $\gtrsim$ 5 Myr (which is consistent with the ages derived by Harris et al 2001, who only find a handful of sources out of a sample of 45 younger than 5 Myr). Lebouteiller et al (2007) show that PAH destruction is only significant when the radiation is hard enough to produce a [S IV]/[Ne II] ratio larger than 1, which only occurs for popula-

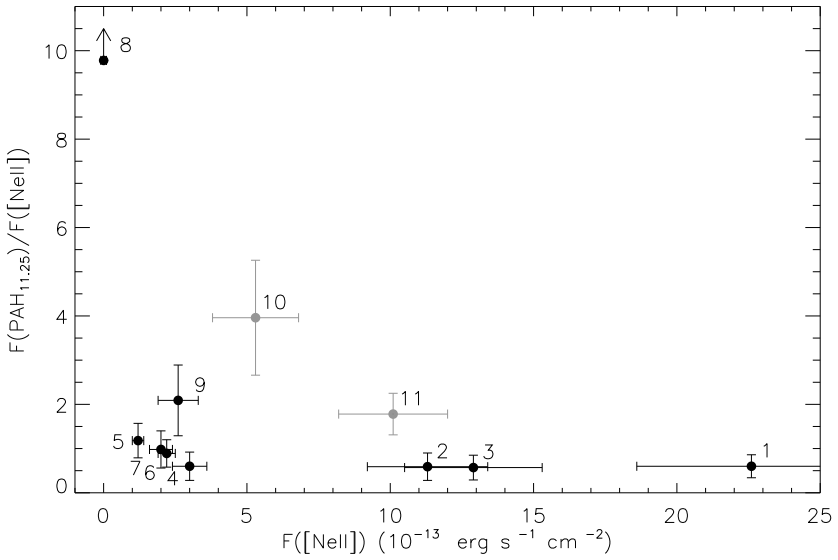

Figure 6.6 — In this diagram the strength of the PAH flux F(PAH$_{11.25\mu m}$) relative to the [Ne II] flux F([Ne II]) is plotted versus F([Ne II]). The black symbols correspond to the compact knots, sources 1 – 9, and the grey to the regions of diffuse emission, sources 10 and 11. The compact knots defined in the [Ne II] map, sources 1 – 7, all have a very similar F(PAH$_{11.25\mu m}$)/F([Ne II]) ratio. The compact sources defined from continuum peaks and the diffuse sources have much stronger PAH emission relative to the [Ne II]emission. Source 8 clearly stands out with a very large F(PAH$_{11.25\mu m}$)/F([Ne II]) ratio.

tions younger than 5 Myr (Fig. 2.9 in Chapter 2). So, the absence of PAH destruction is consistent with more evolved stellar populations dominating the radiation field. Our result also implies that PAH emission as a SFR indicator behaves differently than for instance hydrogen recombination lines, which trace only O and B stars. Measured in small apertures around somewhat evolved clusters, the PAH emission is approximately proportional to the ionizing photon flux. However, integrated over large apertures or even whole galaxies PAH emission is not only sensitive to recent star formation, but has significant contribution from excitation by B, A and probably even later-type stars. Attempts at a quantitative interpretation of the global PAH emission has to take this into account. In a global sense, extragalactic PAH emission contains contributions from dense as well as diffuse ISM components, irradiated by different radiation fields. As long as the ISM structure is comparable and the relative contribution of the diffuse and compact component of PAH emission are similar, calibrations of PAH emission as a SFR indicator integrated over large apertures can be applied. In case of a significantly different ISM, when for example the diffuse component is not present, or, another extreme case, when diffuse matter is the main ISM component, one must take care in inferring a SFR form PAH emission.

The diffuse PAH emission is excited in a different environment than the PAH emission in the compact knots discussed above. It is usually assumed that absorption of UV photons is the dominant excitation mechanism responsible for creating the broad PAH features (Allamandola et al 1985; Draine & Li 2001), which is a good explanation for the compact sources. If a strong UV radiation field would have been responsible for the diffuse component as well, [Ne II] emission would have been detected at these locations. This is not the case. Comparison of the PAH emission with a map of near-infrared molecular hydrogen emission (H_2 1-0 S(1) ro-vibrational line at 2.1218 μm; Fig. 6.5), shows that every location of diffuse PAH emission has H_2 emission associated with it. However, various sources of H_2 emission can be identified that do not have a PAH counterpart. A possible explanation is the fact that ro-vibrational H_2 lines can be excited both thermally and via fluorescence after absorption of a UV photon. In the complex nucleus of M83 we expect both mechanism to be important, with varying contributions, sensitively depending on the characteristics of the local environment. The coexistence of two different excitation mechanism for the molecular hydrogen is probably responsible for the variation in the relative strength of H_2 compared to PAH as well. For example, the brightest peak in the H_2 image, which can be found at the location of the optical nucleus, stands out much more in the H_2 map than the PAH emission from this position. Part of this H_2 emission is likely excited thermally in the shocked gas associated with supernova remnants in this region (Turner & Ho 1994, and Vermaas et al, in preparation). Fluorescent H_2 emission and PAH emission both trace UV-illuminated molecular clouds, but the brightness of the H_2 line is a strong function of density; therefore PAH emission is a cleaner tracer of this process. In a subset of the Spitzer Infrared Nearby Galaxy Survey, Roussel et al (2007) find that on larger scales the H_2 (rotational) line intensities correlate tightly with emission in the PAH bands. Although the distribution of H_2 and PAH emission differ on smaller scales due to density effects, averaged over large aperture (and thus in general sensitive to a lower average density) the two clearly trace the same process. This again indicates that both H_2 and

PAH emission originate from the same locations, predominantly from PDRs.

In general it is remarkable how the structure observed in the [Ne II] map is traced much better by the PAH emission than by H_2. This suggests that indeed thermal excitation is an important mechanism for the production of the H_2 1-0 S(1) line throughout the nucleus of M83. Leaving aside the detailed variations in relative strength, the correlation of the diffuse emission in the PAH and H_2 maps, suggests that the PAH molecules are excited by less energetic photons (e.g. soft UV and optical photons) in PDRs. This is consistent with the findings of Uchida et al (1998) and Li & Draine (2002) on the detection of significant PAH emission in UV-poor nebulae. They conclude that PAH features can be excited by nearby stars with a radiation temperature as cool as T_{eff} = 3000K.

Altogether, this leads to the general picture that the H II regions are most tightly wrapped around the newly formed star clusters. At further distances from the star cluster or in low-excitation environments not directly related to recent massive star formation at all, the PAH molecules are excited by less energetic UV and optical photons (soft enough not to destroy the molecules). From the spatial distribution of the H_2 emission, for example around source 3, it is clear that the H_2 is excited even further out from the region of active star formation, deeper into the PDR than the PAHs. This agrees with observations of the Orion Bar (Fig. 1 in Allers et al 2005; Van der Werf et al 1996; Tielens et al 1993), where PAH emission (the 3.3 μm feature) is observed closer to the young stars than the H_2 1-0 S(1) emission. Besides being excited by UV photons, thermal excitation can be an important mechanism for the H_2 lines as well. We expect the contribution of thermal excitation to the total line emission to be significant in some of the regions in the nucleus of M83, for example in the optical nucleus (source 10). At this location the H_2 emission is very bright, possibly due to the presence of shocked gas near the optical nucleus. However, for PAH molecules the redistribution of energy over the various modes of the molecule after a collision is very fast, so that thermal excitation is not an important excitation mechanism for the observed PAH emission (Tielens 2005).

6.5 Properties of the star-forming regions

To derive various properties of the ionizing stellar populations we use the results of Chapter 2 (Snijders et al, 2007, SKW07 hereafter). In that paper the evolution of the near- and mid-infrared spectral energy distributions (SEDs) of young, embedded star clusters is modeled. The stellar populations plus their surrounding ISM are modeled by combining synthesized SEDs from the stellar population code *Starburst 99 v5.1* (Leitherer et al 1999; Vázquez & Leitherer 2005) with the photoionization code *Mappings IIIr* (Dopita et al 2000, 2002; Groves et al. 2004). The age evolution of a one million $M_\odot$ star cluster, formed in an instantaneous burst with a Salpeter IMF between 0.1 and 100 $M_\odot$, is modeled for various values of metallicity, ionized gas density and of the characteristic ionization parameter of the surrounding dusty nebula. The SEDs are evaluated from 0 – 6 Myr, for metallicities of 0.4, 1 and 2$Z_\odot$. The ionized gas density is varied from 10^2 to 10^6 cm^{-3}. The ionization parameter q is defined as $q = Q_{Lyc}/4\pi R^2 n_{ion}$, with Q_{Lyc} the hydrogen ionizing photon flux, R the distance between

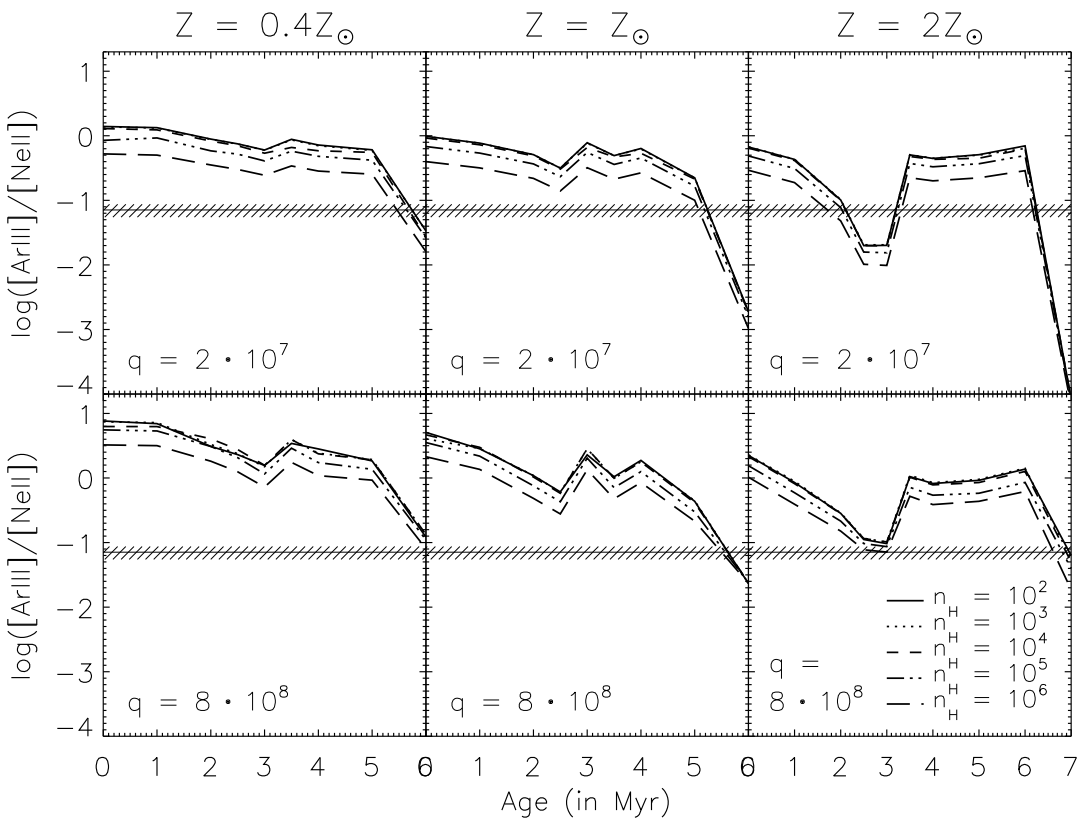

Figure 6.7 — Evolution of the emission line ratio $[\mathrm{Ar\,III}]_{8.99\mu\mathrm{m}}/[\mathrm{Ne\,II}]_{12.81\mu\mathrm{m}}$ with cluster age. The left panels show the curves for Z = 0.4Z$_\odot$, the middle panels Z = Z$_\odot$ and the right panels Z = 2Z$_\odot$. The upper row shows the case of low ionization parameter, $q = 2 \cdot 10^7$ cm s^{-1}, the lower row that of high ionization parameter, $q = 8 \cdot 10^8$ cm s^{-1}. Curves of different line style represent results of models with different densities, ranging from 10^2 cm^{-3} to 10^6 cm^{-3}. The ratio value measured from the spectrum of the central mid-infrared source in the nucleus of M83 is overplotted in all panels (horizontal solid line), the magnitude of the error is indicated by the dashed region.

the radiating source and the inner boundary of the surrounding cloud, and n_{ion} the gas density. The ionization parameter ranges from $2 \cdot 10^7$ cm s^{-1} to $8 \cdot 10^8$ cm s^{-1}. It relates to the commonly used dimensionless ionization parameter U through $\mathrm{U} \equiv 1.1 \cdot q/c$, where the factor 1.1 takes the helium abundance into account (for a more detailed description and examples of the resulting model SEDs, see Chapter 2).

Although we examine line ratios involving two different elements, we do not expect abundance ratios to play a major role, because all mid-infrared fine-structure lines under study here are generated by α–elements (neon, argon and sulphur). All differences in the line ratio behavior with metallicity originate from other processes.

6.5.1 The central star formation complex

In the N-band spectrum of the brightest mid-infrared peak (source 1) two fine-structure lines are detected; strong $[\mathrm{Ne\,II}]_{12.81\mu m}$ and weaker, but clear $[\mathrm{Ar\,III}]_{8.99\mu m}$ emission as well. Since these emission lines have different ionization potentials (27.63 eV for [Ar III] and 21.56 eV for [Ne II]), the line ratio [Ar III]/[Ne II] can be used as a thermometer,

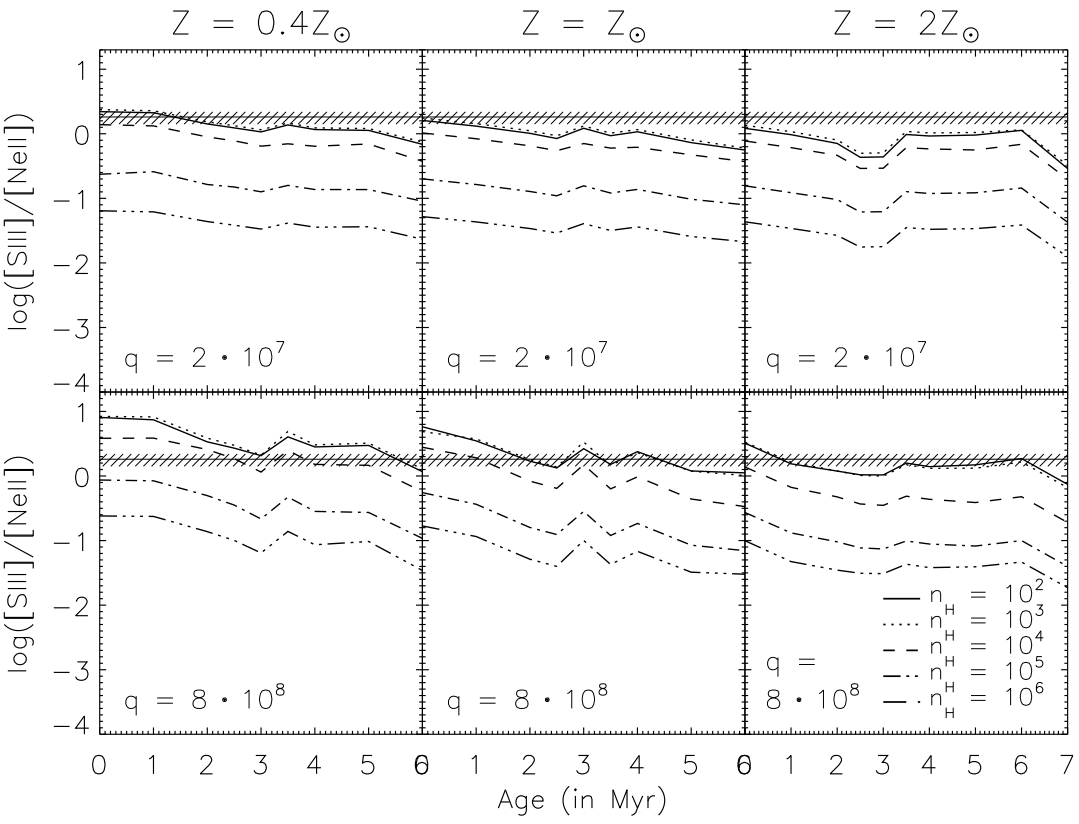

Figure 6.8 — Same as Fig. 6.7, but now for the emission line ratio $[\mathrm{S\,III}]_{18.71\mu\mathrm{m}}/[\mathrm{Ne\,II}]_{12.81\mu\mathrm{m}}$.

measuring the effective temperature of the incoming radiation field. In Fig. 6.7 the measured [Ar III]/[Ne II] emission line ratio is compared with the values predicted by the models (Chapter 2). When the most massive stars evolve off the main-sequence, the cluster's radiation field softens, causing the model curves to drop. With the appearance of the first Wolf-Rayet (W-R) stars at 2 – 3 Myr (depending on metallicity), the radiation field hardens, resulting in an upturn in the predicted ratio value. After the last W-R star disappeared from the stellar population at 5 – 6 Myr, not many energetic photons remain and the ratio drops to zero. In case of solar or subsolar metallicity, the observed line ratio can only be explained by a star cluster in the age range of 5 – 6 Myr. For twice solar metallicity, the modeled line ratio value drops much faster during the initial 2 Myr than those for the $Z_\odot$ and $0.4Z_\odot$ case. High metallicity stars have softer FUV spectra than low metallicity stars of similar mass due to line-blanketing within the stellar atmospheres. This explains the offset towards lower values in the [Ar III]/[Ne II] ratio with increasing metallicity as well as the steeper drop in the ratio in the first 2 Myr. So for $2Z_\odot$ the observed ratio value matches two possible age ranges: 1.5 – 3.3 Myr or 6 – 7 Myr. The upper limit of the [S IV] fine-structure line at 10.51 μm (3σ upper limit: $F_{[\mathrm{S\,IV}]} < 4.9 \cdot 10^{-14}$ erg s^{-1} cm^{-2}) does not help to narrow down the age range or any of the other properties like ionization parameter or ionized gas density. Constraints on the metallicity in M83 do not help to break the age dichotomy either, since Z is determined to be higher than solar, 1.5 – $2Z_\odot$ (based on the strong-line

empirical scale; Zaritsky et al 1994; Kobulnicky et al 1999; Bresolin & Kennicutt 2002, abundances derived from auroral line spectra generally give lower values, and would result in a metallicity closer to solar for M83).

Both age ranges found here agree with the age estimates listed in Harris et al (2001) for the optical sources that can be associated with our source 1. They find two young sources, with ages of 3.0 and 3.5 Myr (their sources 23 and 21), and a handful of sources with ages ranging from 5.1 – 5.9 Myr. Our spectrum most probably has significant contributions from both populations.

Combining the [Ne II]$_{12.81\mu m}$ line with the [S III]$_{18.71\mu m}$ fine-structure line measured in the Q-band spectrum gives us an estimate of the ionized gas density. Since the excitation potentials of the [S III] and [Ne II] emission lines are very similar (23.34 eV and 21.56 eV respectively), the [S III]/[Ne II] ratio is relatively insensitive to the hardness of the radiation. The differences in the critical densities of these two lines ($6.1 \cdot 10^5$ cm^{-3} for [Ne II] and $1.0 \cdot 10^4$ cm^{-3} for [S III]; values for critical densities are obtained from Tielens 2005), makes this ratio very sensitive to the ISM density in the 10^4 – 10^6 cm^{-3} range (Fig. 6.8). Comparison of the curves predicted for [S III]/[Ne II] by the models with the value measured in the spectrum, and taking into account the age and metallicity constraints, we conclude that the density of the ISM is relatively low, $\lesssim 10^3$ cm^{-3}.

There is no clear sign of silicate absorption between 9 – 10.5 μm in the N-band spectrum, indicating that this source suffers little extinction. The measurements from HST images indicate low to intermediate extinction in this region (values found for A_V vary from 0.1 – 1.0 Harris et al 2001).

6.5.2 Source 8

The unresolved source 8 is remarkable, since it is a source of significant PAH and continuum emission, but there is no [Ne II] and no H_2 emission detected (Figs. 6.2 and 6.5). Inspection of Fig. 6.4 shows that source 8 does have optical emission in the F656W filter associated with it. To estimate the Hα flux, we used the data listed in Table 2 in Harris et al (2001). The continuum at 6561 Å was estimated by making a linear interpolation between the F547M and F814W filters. Using the EW(Hα) listed in the table, the Hα flux could be determined ($4.2 \cdot 10^{-13}$ erg s^{-1} cm^{-2}, this value is corrected for an extinction A_V of 0.87). The upper limit on the [Ne II] emission measured in our data is 7.7 $\cdot$ 10^{-15} erg s^{-1} cm^{-2}, thus the ratio of [Ne II]/Hα < 0.02. The SKW07 models predict [Ne II]/Hα < 0.02 for several different cases in the model grid. All these models have ages between 4 – 6 Myr and values for the ionization parameter $\gtrsim 1.6 \cdot 10^8$ cm s^{-1}. The lack of [Ne II] emission in our data can thus be explained by a not too luminous, young star cluster. This is consistent with the modest mass estimate of $48 \cdot 10^3$ M$_\odot$, based on optical images (note that this is one of the two mass estimates given, the second mass is much larger, $\sim 10^6$ M$_\odot$, Harris et al 2001).

However, this leaves the unusually high PAH/[Ne II] ratio of source 8 (see Table 6.2 and Fig. 6.6) unexplained. With a value at least 5 – 15 times larger than the PAH/[Ne II] ratio measured for the other compact knots, source 8 is extraordinarily efficient in producing PAH emission. From HST data Harris et al (2001) mark this object as an interesting source as well. While the EW(Hα) suggests an age of the order

of 6 Myr, the colors indicate a much higher photometric age, around 72 Myr. A deeply embedded, ultradense H II region could possibly produce the mid-infrared observations. At high densities, the dust competes more efficiently with the gas for photons, resulting in a suppression of the fine-structure line emission and a boost of the dust continuum and PAH emission (see Fig.9 in Dopita et al. 2006). However, this does not agree with the low value for the extinction found by Harris et al (2001).

Another possibility is that this source is a low density reflection nebula, ionized by a more evolved stellar population of which all O stars have evolved off the main sequence, leaving B stars as the hottest stars ($\geq$ 7 Myr). Such a star cluster would produce UV photons hard enough to heat the dust and excite the PAH molecules, but too soft to produce very strong fine-structure and recombination lines. Galactic examples of such nebulae are NGC 2023 and NGC 7023, which are illuminated by a B1.5 and a B2 Cepheid variable, respectively. Both nebulae show strong PAH emission (Sellgren et al 1985). In a low density reflection nebula, the dominant mechanism exciting the H_2 lines is fluorescence, dividing the total energy in H_2 emission over a large number of possible ro-vibrational lines (Sternberg & Dalgarno 1989). The flux in the 1-0 S(1) line is then much less than when these low energetic states are thermalized in high density gas, which would explain the absence of significant H_2 1-0 S(1) emission observed here. However, the value measured for the EW(Hα) contradicts a cluster with an age much higher than 6 Myr.

We conclude that the emission measured at position 8 can not easily be understood by a single stellar population. There are most probably contributions of multiple populations of different ages, either closely separated within a small volume (the source size in the mid-infrared data is $\leq$ 18 pc), or more plausible caused by line-of-sight effects. One of these would be young enough to produce the observed Hα emission, the other more evolved and more massive population would be responsible for the optical continuum and the PAH emission.

6.6 Conclusions

In this Chapter, we presented mid-infrared narrowband imaging and spectroscopy of the starbursting nucleus of M83. From a set of five narrowband filters in the N-band a 11.25 μm PAH and a [Ne II] map were constructed. Detailed comparison of these two maps shows that the PAH emission has two components: one correlated with regions of active star formation apparent as peaks in the [Ne II] emission, the other originating from lower-excitation regions, probably related to a thin and patchy veil of dust identified in HST images. The fraction of emission originating from compact star-forming knots relative the total emission from the nucleus of M83 again shows that the [Ne II] emission is more concentrated in the knots than the PAH emission (60 – 80% of the [Ne II] emission originates from the star-forming regions versus 26 – 51% of the PAH total emission). This agrees with the conclusions of Li & Draine (2002), who stated based on the detection of PAH emission in UV-poor nebulae, that PAH molecules can not only be excited by UV photons, but by less energetic photons (soft UV and even optical) as well. Our results imply that PAH emission measured in large apertures is less sensitive to recent star formation than for example Hα or the 24 μm continuum.

In the central region of M83 49% – 74% of the total PAH emission is probably excited by more evolved B, A or even later type stars, and the contribution of diffuse PAH emission likely grows with increasing aperture radius. Studies of PAH emission integrated over large apertures or whole galaxies have to take this into account. In such large apertures, extragalactic PAH emission contains contributions from dense as well as diffuse ISM components, irradiated by different radiation fields. At the distance of M83, high spatial resolution data can resolve H II/PDR complexes, and it is possible to zoom in on individual star-forming regions. Interpretation of the observations is not straightforward due to the complex and varying morphology of the two components of PAH emission. Our ground-based, high spatial resolution imaging data thus show that PAH emission can be used as a star formation rate (SFR) indicator, as long as the ISM structure of the object under study is similar to that of the object used for the calibration of the SFR as a function of PAH emission.

From the observed features in the N- and Q-band spectra, we conclude that the brightest mid-infrared source suffers little extinction. The stellar population responsible for this mid-infrared emission has an age in the range of 1.5 – 3.3 Myr or 6 – 7 Myr, assuming a metallicity of $2Z_{\odot}$. Close inspection of HST images of this region shows that a handful of clusters is identified in the optical, so the spectral energy distribution most probably arises from a combination of several stellar populations. The density of the ionized gas surrounding the stellar populations is relatively low, $\lesssim 10^3$ cm^{-3}.

Acknowledgments

We thank the Paranal Observing Team for their support. Furthermore, we are very grateful to Jan Willem Pel for his tireless efforts over the last decade in building VISIR and supporting its users.

References

Allamandola, L. J., Tielens, A. G. G. M. & Barker, J. R., 1985, ApJ 290, L25
Allers, K. N., Jaffe, D. T., Lacy, J. H., Draine, B. T. & Richter, M. J., 2005, ApJ 630, 368
Black & Van Dishoeck
Bresolin, F. & Kennicutt, R. C., 2002, ApJ 572, 838
Bonnet, H. et al., 2004, The ESO Messenger 117, 17
Caldwell, N., & Phillips, M. M., 1989, ApJ 338, 789
Calzetti, D., Meurer, G. R., Bohlin, R. C., Garnett, D. R., Kinney, A. L., Leitherer, C. & Storchi-Bergmann, T., 1997, AJ 114, 1834
Calzetti, D., Conselice, C. J., Gallagher, J. S. & Kinney, A. L.,1999, AJ 118, 797
Calzetti, D. et al., 2007, in press (arXiv:0705.3377)
Churchwell, E., 2002, ARA&A 40, 27
Cohen, M., Walker, R. G., Carter, B., Hammersley, P., Kidger, M. & Noguchi, K., 1999, AJ 117, 1864
Devillard, N., 1997, The Messenger 87, 19
Dopita, M. A., Kewley, L. J., Heisler, C. A. & Sutherland, R. S., 2000, ApJ 542, 224
Dopita, M. A., Groves, B. A., Sutherland, R. S., Binette, L. & Cecil, G., 2002, ApJ 572, 753
Dopita, M. A. et al., 2006, ApJ 639, 788
Draine, B. T., 1989, in ESLAB Symp. 22, IR Spectroscopy in Astronomy, ed. B. H. Kaldeich, ESA SP-290, 93
Draine, B. T., & Li, A., 2001, ApJ 551, 807
Eisenhauer, F. et al., 2003, SPIE 4841, 1548

Elmegreen, D. Meloy, Chromey, F. R. & Warren, A. R., 1998, AJ 116, 2834
Gallais, P., Rouan, D., Lacombe, F., Tiphene, D. & Vauglin, I., 1991, A&A 243, 309
Gao, Y. & Solomon, P., 2000, BAAS 197, 9603
Gilbert, A. M. et al, 2000, ApJ 533, 57
Groves, B. A., Dopita, M. A. & Sutherland, R. S., 2004, ApJS 153, 9
] Harris, J., Calzetti, D., Gallagher, J. S., Conselice, C. J. & Smith, D. A., 2001, AJ 122, 3046
Huchtmeier, W. K. & Bohnenstengel, H.-D., 1981, A&A 100, 72
Hummer, D. G. & Storey, P. J., 1987, MNRAS 224, 801
Kobulnicky, H. A., Kennicutt, R. C. & Pizagno, J. L., 1999, ApJ 514, 544
Lagage, P. O. et al, 2004, The Messenger 117, 12
Lebouteiller. V., Brandl, B., Bernard-Salas, J., Devost, D. & Houck, J. R, 2007, in press (arXiv:0704.2068)
Leitherer C. et al, 1999, ApJS 123, 3
Li, A. & Draine B. T., 2002, ApJ 572, 232
Lorenz et al, 1993, A&A 277, 321
Mengel, S., Lehnert, M. D., Thatte, N., Tacconi-Garman, L. E. & Genzel, R., 2001, ApJ 550, 280
Mengel, S., Lehnert, M. D., Thatte, N. & Genzel, R., 2005, A&A 443, 41
Mirabel, I. F. et al. 1998, A&A 333, L1
Moorwood A. et al, 1998, The Messenger 94, 7
Park, O.-K., Kalnajs, A., Freeman, K. C., Koribalski, B., Staveley-Smith, L. & Malin, D. F., 2001, in ASP Conf. Ser. 230, Galaxy Disks and Disk Galaxies, eds. J. G. Funes & E. M. Corsini (San Francisco: ASP), 109
Pérez-González, P. G., et al, 2006, ApJ 648, 987
Perryman, M. A. C. et al., 1997, A&A 323, 49
Rosenthal, D., Bertoldi, F. & Drapatz, S., 2000, A&A 356, 705
Roussel, H., et al., 2007, in press (arXiv:0707.0395)
Sellgren, K., Allamandola, L. J., Bregman, J. D., Werner, M. W. & Wooden, D. H., 1985, ApJ 299, 416
Shull, J. M. & Hollenbach, D. J., 1978, ApJ 220, 525
Saviane, I., Hibbard, J. E. & Rich, M. R., 2004, AJ 127, 660
Snijders L., Van der Werf, P. P., Brandl, B. R., Mengel, S., Schaerer, D. & Wang, Z., 2006, ApJ 648, 25
Snijders L., Kewley, L. J. & Van der Werf, P. P., 2007, in press (arXiv:0707.1397)
Sternberg, A. & Dalgarno, A., 1989, ApJ 338, 197
Telesco, C. M., 1988, ARA&A 26, 343
Thatte, N., Tecza, M., & Genzel, R., 2000, A&A 364, L47
Thim F., Tammann, G. A., Saha, A., Dolphin, A., Sandage, A., Tolstoy, E. & Labhardt, L., 2003, ApJ 590, 256
Tielens, A. G. G. M., Meixner, M. M., Van der Werf, P. P., Bregman, J., Tauber, J. A., Stutzki, J. & Rank, D., 1993, Science 262, 86
Tielens, A. G. G. M., 2005, The Physics and Chemistry of the Interstellar Medium (Cambridge University Press)
Timmermann, R., Bertoldi, F., Wright, C. M., Drapatz, S., Draine, B. T., Haser, L. & Sternberg, A., A&A 315, 281
Tremonti, C. A., Calzetti, D., Leitherer, C. & Heckman, T. M., 2001, ApJ 555, 322
Turner, J., Kirby-Docken, K. & Dalgarno, A., 1977, ApJS 35, 281
Turner, J. & Ho, P. T. P, 1994, ApJ 421, 122
Uchida, K. I., Sellgren, K., & Werner, M. W., 1998, ApJ 493, L109
Vázquez, G. A. & Leitherer C., 2005, ApJ 621, 695
Vogler, A., Madden, S. C., Beck, R., Lundgren, A. A., Sauvage, M., Vigroux, L. & Ehle, M, 2005, A&A 441, 491
van den Bergh, S., 1980, PASP 92, 122
Van der Werf, P. P., Stutzki, J., Sternberg, A. & Krabbe, A., 1996, A&A 313, 633
Whitmore, B. W. & Schweizer, F., 1995, AJ 109, 960
Wolniewicz, L., Simbotin, I. & Dalgarno A., 1998, ApJS 115, 293
Zaritsky, D., Kennicutt, R. C. & Huchra, J. P., 1994, ApJ 420, 87